Received: 26 January 2021 | Revised: 29 March 2021 | Accepted: 3 April 2021

DOI: 10.1111/jace.17845

Journal of the American Ceramic Society

ORIGINAL ARTICLE

Influence of oxygen vacancies on core-shell formation in solid solutions of (Na,Bi)TiO_3 and $SrTiO_3$

Sebastian Steiner[1] | **Jonas Heldt**[1] | **Oded Sobol**[2] | **Wolfgang Unger**[2] | **Till Frömling**[1]

[1]Department of Materials and Earth Science, Technical University of Darmstadt, FG Nichtmetallisch-Anorganische Werkstoffe, Darmstadt, Germany

[2]Bundesanstalt für Materialforschung und -prüfung (BAM, Berlin, Germany

Correspondence
Till Frömling, Department of Materials and Earth Science, Technical University of Darmstadt, FG Nichtmetallisch-Anorganische Werkstoffe, Alarich-Weiss-Straße 2, Darmstadt 64287, Germany.
Email: froemling@ceramics.tu-darmstadt.de

Funding information
Deutsche Forschungsgemeinschaft, Grant/Award Number: FR 3718/1-1 and UN 80/14-1

Abstract

Solid solutions of (Na,Bi)TiO_3 (NBT) and $SrTiO_3$ (ST) are materials of interest for high-strain or high-energy density capacitor applications. Often, they exhibit chemical heterogeneity and develop core-shell structures during regular solid-state synthesis with an NBT-rich core. In this case, the NBT forms first so that the strontium needs to diffuse into the material to reach chemical homogeneity. Depending on the presence of core-shell structures, the electrical properties can vary drastically. In this work, we rationalize the effect of variations in oxygen vacancy concentration by Fe-acceptor and Nb-donor doping. It can be shown that a diffusion couple of strontium and oxygen is responsible for chemical homogenization and that the oxygen vacancy content can control the formation of a core-shell structure.

KEYWORDS

bismuth titanates, core-shell structures, diffusion/diffusivity, ferroelectricity/ferroelectric materials, lead-free ceramics

1 | INTRODUCTION

Chemical heterogeneity in the form of core-shell structures can develop in lead-free ($Na_{1/2}Bi_{1/2}$)TiO_3 (NBT)-based and ($K_{0.5}Na_{0.5}$)NbO_3 (KNN)-based ceramics during a regular solid-state sintering process.[1,2,3,4,5,6] These can have a high impact on electric and ferroelectric properties. Even in pure KNN, core-shell material can form depending on the type of Nb-oxide used as an educt.[5] In the case of NBT, solid solutions with $SrTiO_3$ (ST) are especially prone to result in heterogeneous compositions.[7]

NBT solid solutions with ST (NBT-ST) are of particular interest for high strain ferroelectric applications.[2,4,8,9,10,11,12,13] Strains above 0.3% could be achieved. Furthermore, the polarization hysteresis loops (polarization P plotted vs. electric field E) show pinching with low remanent polarization. This is potentially interesting for high-energy storage capacitor applications, as this behavior is similar to an anti-ferroelectric.[14,15] High energy density could be stored compared to regular polar dielectrics.

The origin of the properties is still unclear. No proof of actual anti-ferroelectricity could be shown in these types of materials. The work by Koruza et al,[2] Liu et al,[4] and Molina-Luna et al,[8] however, introduced an exciting hypothesis. They elucidated the existence of the core-shell structure in NBT-25ST and could show that the shell is ST rich while the core is rather pure NBT. Thus, it is possible that with the applied electric field, the non-ergodic NBT core could undergo a field-induced relaxor-ferroelectric phase transition while the ergodic shell does not. With the removal of the electric field, the shell is driven back to the equilibrium, influencing the core material to do so as well and revert to the relaxor state. Hence, the remanent polarization is reduced. This could even be illustrated using field-dependent TEM. Interestingly, even

at temperatures around 800 K, a ferroelectric-like polarization could be induced in such a core-shell structure, which was ultimately attributed to a flexoelectric effect.[8] The problem with that theory, however, is that the literature about NBT-ST derived compositions often does not report core-shell structures[9,10,11,12,16,17,18,19,20,21,22,23,24,25,26,27] or specifically states that is non-present.[28,29] Therefore, it is of high importance to rationalize the formation and impact of core-shell structures in the respective materials.

It could recently be shown that the material with 25 mol% ST content (NBT-ST) obtains significantly different electrical and ferroelectric properties depending on the presence of a core-shell structure.[7] The formation of a core-shell material could simply be tuned by varying the stoichiometry of the bismuth. With Bi-deficiency, we expect to induce bismuth and oxygen vacancies:

$$2Bi_{Bi}^{x} + O_{O}^{x} \rightarrow 2V_{Bi}^{'''} + 3V_{O}^{\cdot\cdot} + Bi_2O_3 \uparrow . \quad (1)$$

The higher the respective vacancy concentrations, the higher the chemical diffusion coefficient to allow for reaching chemical homogeneity. Therefore, Bi-enriched (core-shell) and Bi-deficient (no core-shell) samples had significantly different microstructures and functional properties. The chemically homogeneous Bi-deficient samples behaved like regular ferroelectrics with low maximum strain and high remanent polarization. Thus, this hints towards at least a correlation of the core-shell structures with high strain and pinched ferroelectric loops.

Concerning the formation of the core-shell structure, it could be rationalized that NBT is formed first during calcination. It was hypothesized that the Sr diffuses via a vacancy mechanism on the A-site vacancies into the NBT, and its diffusion is coupled to the Na/Bi diffusion.[7] Therefore, the higher amount of $V_{Bi}^{'''}$ should lead to a faster homogenization of the ceramic. However, NBT materials are very sensitive to the presence of oxygen vacancies.[30,31,32,33,34] It could be shown that oxygen ionic conductivity changes non-linearly with increasing acceptor doping and oxygen vacancy concentration. This leads to low intrinsic electronically conductive samples for low oxygen vacancy concentration. Chances by only about 0.1% in vacancy content can then lead to dominating oxygen conductivity (transport coefficient >90%). Evidence could be provided that this results from a concentration-dependent defect couple formation between acceptor species (which could also be $V_{Bi}^{'''}$) and oxygen vacancy.[33,34,35,36] It leads to much more free and mobile oxygen vacancies causing changes by orders of magnitude in conductivity by only small vacancy concentration variations. Therefore, we will elucidate the effect of doping on core-shell development in this work. The introduction of Nb-donor doping or Fe-acceptor doping and bi-stoichiometry variations allows for changing the oxygen vacancy concentration without impacting the bismuth vacancy concentration. For example, the oxygen vacancy concentration can be increased with Fe-acceptor doping, while Bi enrichment leads to a low Bi-vacancy concentration. Introducing Nb doping and an additional Bi deficiency causes a high Bi-vacancy content and low oxygen vacancy concentration at the same time. With this, we are able to elucidate the defects dominating the sintering kinetics and provide suggestions for tuning and controlling the functional properties of NBT-ST and related compositions.

2 | EXPERIMENTAL

Bulk pellets of 0.75 $(Na_{1/2}Bi_x)TiO_3$-0.25$SrTiO_3$ (NB_xT-25ST) ceramics with compositional range of $0.495 < x < 0.505$ were prepared by a conventional solid-state method. Additionally, samples with the Bi-stoichiometry variation of $0.49 < x < 0.51$ were 3% wt. Fe acceptor (3Fe-NB_xT-ST) or 3% wt. Nb-donor doped (3Nb-NB_xT-ST). Powdered Bi_2O_3, Na_2CO_3, TiO_2, Fe_2O_3, or Nb_2O_5 (>99%, Alfa Aesar GmbH, Karlsruhe, Germany) and $SrCO_3$ (Sigma-Aldrich, St. Louis, Missouri, USA) were mixed for 24 hours with zirconia balls and ethanol using a planetary ball mill (Fritsch Pulverisette 5, Idar-Oberstein, Germany). After drying, the powder mixture was calcined at 750°C for 2 hours (heating rate of 5 K/min). The calcined powder was re-milled for 24 hours. The powders were pressed into discs with a uniaxial pressure of 127 MPa and pressed isostatically at 300 MPa. The green bodies were sintered at 1,150°C for 2 hours (5 K/min heating and cooling rate. The density measurements of the produced samples were done following the Archimedes' principle for three samples of each composition. The specimens' structural properties were investigated by X-ray diffraction (XRD; AXS D8; Bruker Corporation, Karlsruhe, Germany). After coating the samples with carbon by sputtering deposition, secondary electron microscopy (SEM) images backscattered electron (BSE) images were recorded with an SEM (Philips XL30FEG; Philips, Amsterdam, Netherlands). The grain size has been calculated from the SEM images by using the software LINCE, V. 2.4.2 (Sergio Luis dos Santos e Lucato, Nichtmetallisch-Anorganische Werkstoffe, TU Darmstadt, Germany), taking into account about 300 grains. The program is based on the linear intercept method according to ASTM E 112-95. Additionally, time-of-flight secondary mass spectrometry (ToF-SIMS; TOF-SIMS IV, IONTOF, Münster, Germany) was conducted to investigate the cation interdiffusion for the samples, which showed a different contrast in the BSE images. Measurements were performed using a liquid metal ion gun (LMIG) with a BiMn source to provide a 25 kV Bi^{+1} primary ion beam. Analyses were carried out in the collimated burst alignment (CBA) to enable a sufficient lateral resolution on a selected region of interest

(ROI) in the size of 80 × 80 μm.[37] Additionally to the LMIG, a dual-source column (DSC) with 1 kV O^+ ions was operating to perform depth profiling and ablation of the sample surface. The use of oxygen ions enabled the removal of surface contaminations and the enhancement of ionization probability of the positive secondary ions. The raster size of the sputter gun was adjusted to 300 × 300 μm. Low-energy electron flood gun was used constantly to overcome surface charging during sputtering and analysis. The flood gun was adjusted according to the recommended procedure by IONTOF.

For electrical measurements, Pt electrodes were sputtered on both surfaces of the disc-shaped samples after grinding and polishing down to 0.25 μm with a Pheonix 4000 (Buehler, Esslingen, Germany). The large signal properties, such as polarization loops and strain curves, were measured with the aixPSE system (aixACCT system GmbH, Aachen, Germany) at 0.5 Hz. The permittivity and the dielectric loss were measured with an HP 4284A (Hewlett Packard Corporation, Palo Alto, USA) at 1 kHz, 10 kHz, 100 kHz, and 1 MHz. Impedance spectroscopy was conducted with the Alpha-A High-Performance Frequency Analyzer (Novocontrol Technologies, Montabaur, Germany) at different temperatures (150-700°C, 25 K steps, and 5 K/min heating rate). The amplitude was 0.1 V, and the frequency range was 0.1 Hz to 3 MHz. The obtained spectra were analyzed with the software RelaxIS (RHD instruments, Darmstadt, Germany).

3 | RESULTS AND DISCUSSION

3.1 | Investigation of chemical heterogeneity

Previously, the detection of core-shell structures was rationalized with BSE and ToF-SIMS measurements.[2,4,7] The question is whether regular XRD could also give information on the presence of this chemical heterogeneity. It is usually seen to be able to detect secondary phases if the content is higher than 2% and its crystal structure is significantly different. The diffractograms of the respective materials are depicted in Figure 1.

The compositions exhibit a pseudocubic crystal structure typical for ABO_3 relaxor perovskites. Rietveld refinement with a cubic fit of space group $Pm\bar{3}m$ was performed, and the obtained lattice constants are all in the range of 3.9 Å. The pseudocubic phase and the obtained lattice parameters are in good agreement with the literature.[1,13,38,39] However, some publications declare that the crystal structure of NBT-25ST has a small tetragonal distortion.[17,40]

The (200) peak shows a shoulder at lower angles for all compositions. This can best be observed in NBT-25ST and $NB_{0.495}$T-25ST (see Figure S1). This peak splitting may indicate a minor tetragonal distortion, leading to a peak split of the (200) and (002) peaks. Hence, Rietveld refinement was carried out with the tetragonal space group P4bm. The obtained lattice parameters are given in Table S1. Note that for

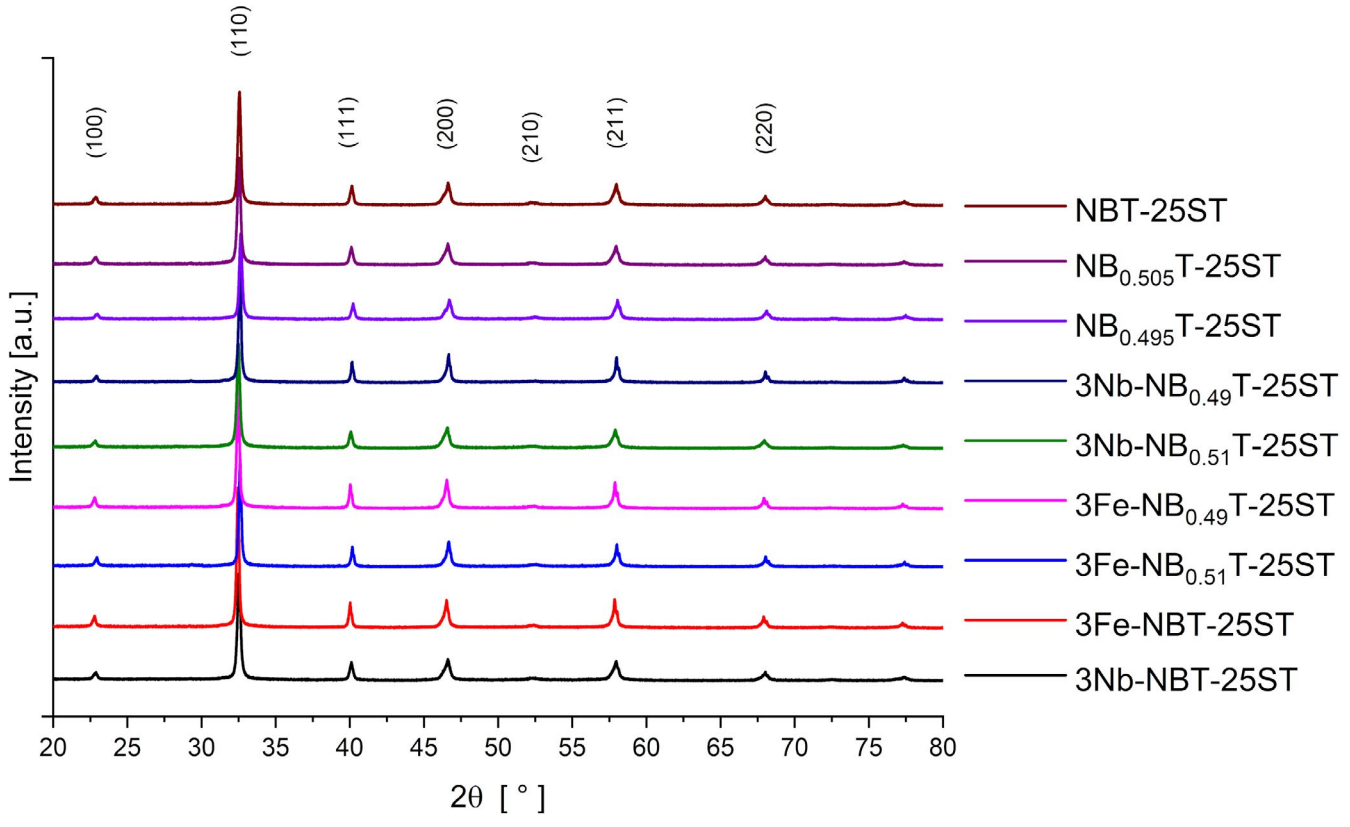

FIGURE 1 XRD results of NBT-ST based compounds

this calculation, the cubic unit cell is used to allow for easier comparison. The average elongation of the *c* axis by 0.381% compared to the *a* axis is, nevertheless, small. Furthermore, the splitting of the (200) peak in NBT-25ST could also originate from the coexistence of rhombohedral and pseudocubic phases.[39] There is also peak splitting at higher angles for the (211) and (220) peaks (not shown). These can be rationalized with Cu Kα radiation consisting of a duplet Kα1 and Kα2, which have a slightly different wavelength.

Previous work by Acosta et al[1] illustrated that core-shell structures in NBT-25ST have a coherent or semicoherent interface between the core and shell. Therefore, a Rietveld refinement of these materials should only detect a single phase with a strain gradient. The obtained lattice parameters and the (200) peak irregularities could thus not be correlated with the presence of core-shell microstructure. This could also explain why a core-shell structure is not detected in many previous works. It is important to use advanced characterization techniques like ToF-SIMS, EDX, and BSE to elucidate the presence of a core-shell structure.

A chemical heterogeneity does not become evident from SEM images, as well. In Figure 2, the results of pure NBT-ST, 3Fe-NBT-ST, and 3Nb-NBT-ST are illustrated. The microstructure, nevertheless, shows different grain sizes for the three materials. The largest average grain size results for the acceptor doped 3Fe-NBT-ST (15.5 μm), while slow grain growth occurs for the donor doped 3Nb-NBT-ST (1 μm). This is in accordance with previous results on NBT and NBT solid solutions with $BaTiO_3$. For these materials, acceptor doping results in a fast grain growth due to oxygen vacancies modifying the grain boundary properties.[34] The $NB_{0.505}$T-ST Bi-enriched sample has a small average grain size (1.2 μm; supporting information; Figure S2A), which is in a similar range as 3Nb-NBT-ST. The Bi-deficient $NB_{0.495}$T-ST obtains an average grain size of 7.7 μm (Figure S2B). Both can again be correlated with the presence of low or high oxygen vacancy concentration, respectively. Note that Bi excess and Bi deficiency only lead to small variations for the doped samples. However, there is a decrease in grain size for Bi-excess material. Furthermore, there is limited grain growth for 3Fe-$NB_{0.49}$T-ST (Figure S2F). In this case, secondary phases might influence the grain boundary diffusion mechanisms and change the resulting grain size.[34] Only small changes in the density could be determined for the samples in this work, despite the significantly different grain sizes. The ceramics exhibit densities from 95-99%.

The presence of core-shell structures could finally be elucidated with BSE and ToF-SIMS investigations. The small brighter areas in Figure 3 can be attributed to the cores of the core-shell structure. The concentration of the heavy element bismuth is higher in the core than in the shell, where it is diluted by lighter strontium. Since heavier elements backscatter electrons more strongly than light elements, a contrast between core and shell develops. The observed sizes of the cores are roughly 200-400 nm, and they are only visible in some grains. Compared to the stoichiometric NBT-25ST, the amount of visible cores increases for the bismuth enriched $NB_{0.505}$T-25ST.

Nearly every grain possesses a core in $NB_{0.505}$T-25ST. These findings match with previously reported results.[7] All Nb-doped compositions showed the existence of core-shell microstructures as well. In contrast to this, core-shell structures were not visible in Fe-doped compositions. Similar results as for the BSE measurements could be obtained from the ToF-SIMS investigations. In Figure 4, the intensity of Ti and Sr cations is given for $NB_{0.505}$T-25ST and 3Nb-$NB_{0.49}$T-25ST. Pores and pinholes give a dark contrast also for the Ti-cation signal in Figure 4A,C. From Figure 4B,D, it becomes evident there are additional regions of dark contrast for the Sr-intensity. These can be attributed to the Sr-deficient cores.[7] The core-shell structure is best visible in the $NB_{0.505}$T-25ST results, which also agrees with the BSE images in Figure 3B. For NBT-25ST, only a few cores could be determined. These images are given in Figure S4. Previous studies showed a better resolution of the cores.[7] However, in the present case, these regions' size is smaller and only a few hundred nanometers in diameter. The ToF-SIMS instrument's resolution in the respective CBA mode is roughly 100 nm. Nevertheless, the results clearly illustrate the existence of core-shell structures in the respective samples.

Excess bismuth in 3Nb-$NB_{0.51}$T-25ST seems to increase the amount of core-shell structures even further compared to the bismuth deficient 3Nb-$NB_{0.49}$T-25ST in the BSE images Figure 3. It is thus the sample with the highest density of cores. However, the core sizes are the smallest and could

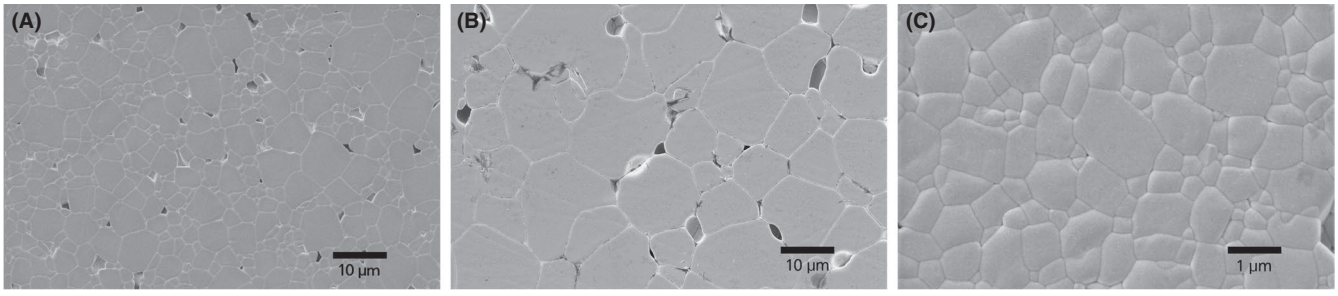

FIGURE 2 SEM images of (A) stoichiometric NBT-ST, (B) 3Fe-NBT-ST, and (C) 3Nb-NBT-ST

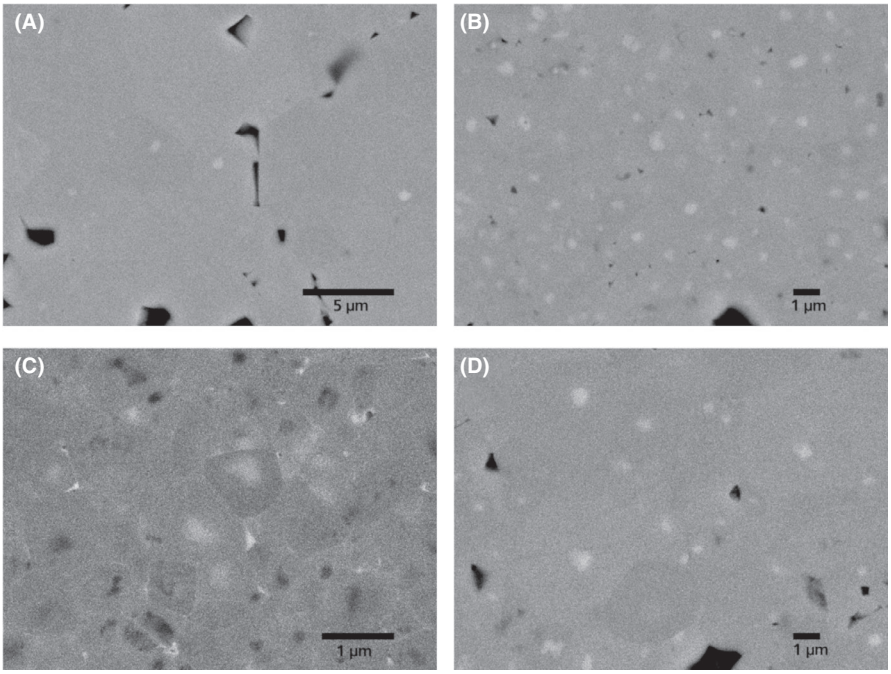

FIGURE 3 BSE results of materials containing core-shell structures. (A) NBT-25ST; (B) $NB_{0.505}$ T-25ST; (C) 3Nb-$NB_{0.51}$ T-25ST; and (D) 3Nb-$NB_{0.49}$ T-25ST

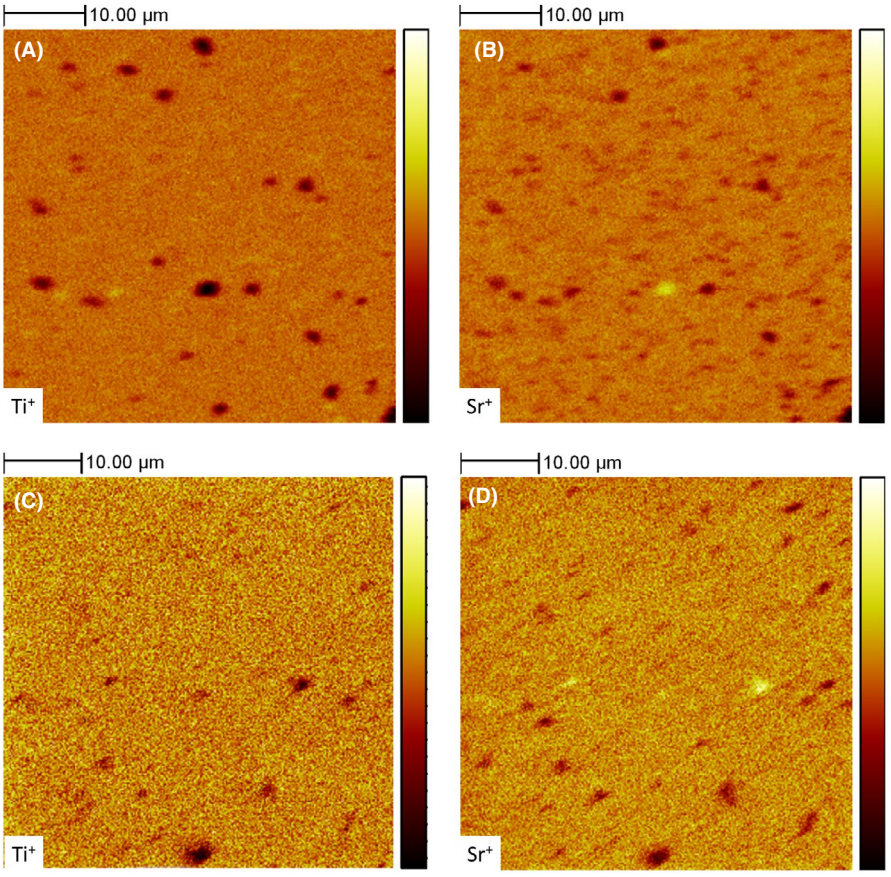

FIGURE 4 (A) Ti and (B) Sr cation distribution from SIMS data of $NB_{0.505}$ T-25ST. (C) Ti and (D) Sr cation distribution from SIMS data of 3Nb-$NB_{0.495}$ T-25ST. Intensity increases according to the color scale on the right of the images

not be resolved in the ToF-SIMS experiments. These results could mean that Bi vacancies have an influence on the microstructure. However, the BSE image for 3Nb-$NB_{0.51}$T-25ST in Figure 3C shows bright regions where grain boundaries can be identified. This hints towards the formation of a Bi-rich secondary phase. For the 3Nb-$NB_{0.49}$T-25ST, no secondary phase was detected at the grain boundaries but has been found in similar Bi-deficient compositions.[31] Therefore, the difference in Bi-vacancy concentration may not be as high as 1% of the available A-site positions for the two samples.

To rationalize the impact of oxygen vacancies, the comparison between NB_{495}T-ST and 3Nb-$NB_{0.49}$T-ST is important. Despite most likely having more A-site vacancies than NB_{495}T-ST, the 3Nb-$NB_{0.49}$T-ST exhibits small grains and the development of a prominent core-shell structure. Hence, the A-site vacancies are not the decisive factor for core-shell formation. Therefore, the presence of oxygen vacancies seems to significantly influence the components' chemical homogeneity. Experimental proof of the presence of oxygen vacancies and their influence on functional properties will be rationalized in the following chapter on the electrical properties of the ceramics.

3.2 | Electrical properties

With the help of impedance spectroscopy, the changes in conductivity/dielectric loss can be illustrated, and the dominant mobile charge carriers can be derived.[41] The stoichiometric NBT-ST, Bi-enriched, and donor doped samples all have similar properties. They show high resistance with one single semi-circle in the Nyquist-plots for the bulk process and no electrode response (Figure 5A). This hints towards dominating electronic conductivity. The acceptor doped and Bi-deficient samples can exhibit up to three responses and an overall multiple orders of magnitude lower resistance (Figure 5B,C). This is in accordance with the results for pure NBT and NBT-BT.[30,33,34] A non-linear dependency between oxygen vacancy concentration and oxygen conductivity could be found in these cases. This can be further elucidated by discussing the Arrhenius-plots of conductivity and the conduction mechanisms' respective activation energy.

The low conductive samples in Figure 6 show only minor deviations in conductivity over a large temperature range. The activation energies are about 1.6 eV, which is half the bandgap of regular NBT and most likely also of NBT-ST. Therefore, we can safely assume intrinsic electronic conductivity.[30] The highly conductive samples in Figure 6 behave very similarly to acceptor doped NBT and NBT-BT. In these cases, it could be proven with electromotive force measurements that dominant oxygen ionic conductivity (ionic transfer coefficient >90%) is present, which even rivals yttria-stabilized zirconia.[30,34] The high-temperature oxygen ionic conductivity increases by multiple orders of magnitude. The results are clear evidence for the correlation between the presence of core-shell structures with high oxygen ionic vacancy concentration and mobility. In a previous publication, we hypothesized that the homogenization of the material is determined by the diffusion of Sr, coupled with the diffusion of Na and Bi.[7] This work illustrates that the couple dominating chemical diffusion is rather strontium ions and oxygen vacancies. The non-linearity of the oxygen vacancy transport seems to responsible for the drastic changes in chemical homogeneity and thus also in electrical properties. At lower oxygen vacancy concentration, the mobility is also low, and hence, chemical diffusion is dominated by them. The vacancies are much more mobile at high oxygen vacancy concentration, facilitating a fast homogenization of the samples. The grain growth process and its correlation to the oxygen vacancy concentration nevertheless need to be further investigated to fully describe the core-shell formation. Nevertheless, it becomes clear that the key to controlling the core-shell structure development is the oxygen vacancy concentration.

The increase in conductivity is also reflected in the dielectric loss from permittivity measurements (Figure 7). The acceptor doped and oxygen-deficient samples all exhibit a high loss in the high-temperature range, which can be seen as the increase in the contribution from mobile oxygen vacancies. This furthermore also affects the real part of the permittivity in this temperature range. Such a behavior is commonly observed for lossy material with multiple processes contributing to the overall electrical response.[42,43] Depending on the chosen limited set of frequencies, the response does not reflect the bulk process's permittivity but a grain boundary or electrode process. For the donor doped and Bi over-stoichiometric samples, the dielectric loss decreases, but there is also a decrease in maximum permittivity in Figure 7. Overall, the stoichiometric NBT-ST properties do, nevertheless, not differ significantly from the donor-doped

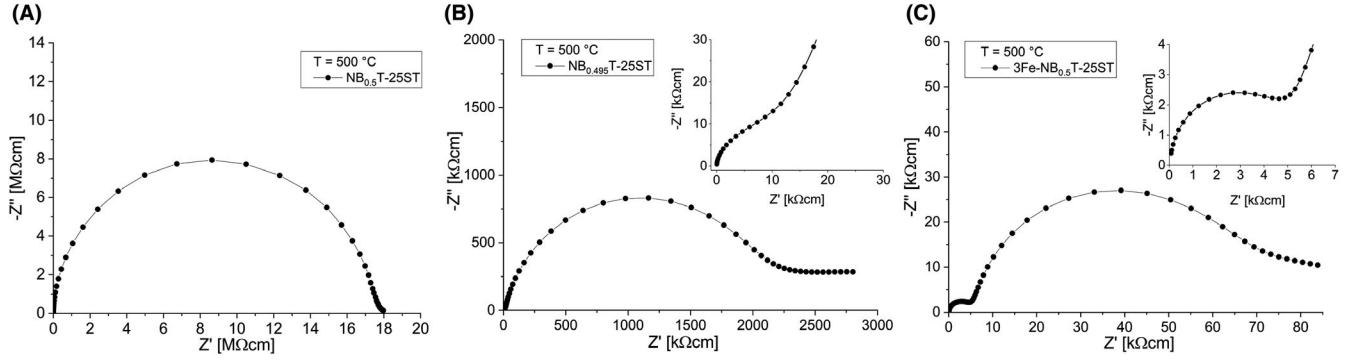

FIGURE 5 Representative Nyquist-plots of the ceramics from impedance measurements. (A) NBT-25ST, (B) $NB_{0.495}$ T-25ST, and (C) 3Fe-NBT-25ST

samples. Further plots of temperature dependent permittivity and dielectric loss can be found in Figures S5-S7. The acceptor doped ceramics exhibit much more pronounced differences resulting from the mobile oxygen vacancies. However, it seems that room temperature losses are almost similar even for the acceptor doped ceramics. Therefore, it is expected that the ferroelectric properties can still be rationalized for all samples.

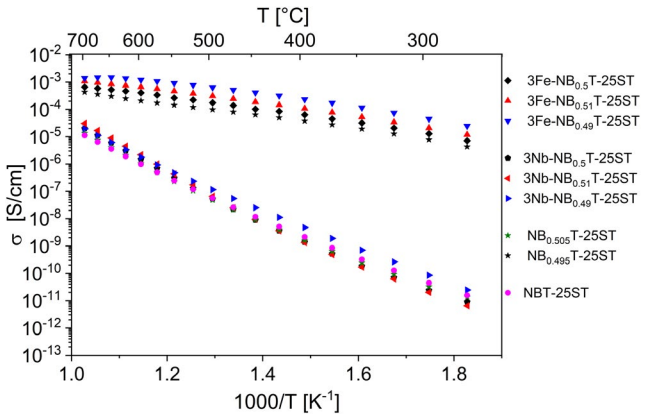

FIGURE 6 Arrhenius-plots of NBT-ST based ceramics

The comparison of the PE-plots of the Bi-stoichiometry variation in undoped NBT-ST (Figure 8A) illustrates that the remanent polarization decreases with Bi-enrichment. Therefore, the pinching of the loops correlates with the presence of a core-shell structure in this case. This can also be derived from the field-dependent strain (Figure 8B), where the $NB_{0.495}$T-ST exhibits ferroelectric behavior while the others act like relaxor materials with only small negative strain components. Note that the maximum strain is reached for the stoichiometric NBT-25ST, which hints towards saturation of Bi in the lattice. A Bi-enrichment in the educts may account for Bi evaporation, but any Bi in excess could form secondary phases impacting the electrical properties. However, such a grain boundary secondary phase could only be found for 3Nb-$NB_{0.51}$T-25ST in this work. It has, nevertheless, also been reported in previous publications.[34] For the Fe-doped samples, an excess of Bi also does not change the properties significantly compared to the stoichiometric sample (Figure 8C). The 3Fe-$NB_{0.495}$T-25ST, however, exhibits a higher coercive field (Figure 8C) and a lower maximum strain (Figure 8D). This slight hardening of ferroelectric properties is similar to what has been observed for acceptor doped NBT-BT, where acceptor doping had the same effect.[34] Note that the PE-loops of the 3Fe-NBT-25ST are not that different

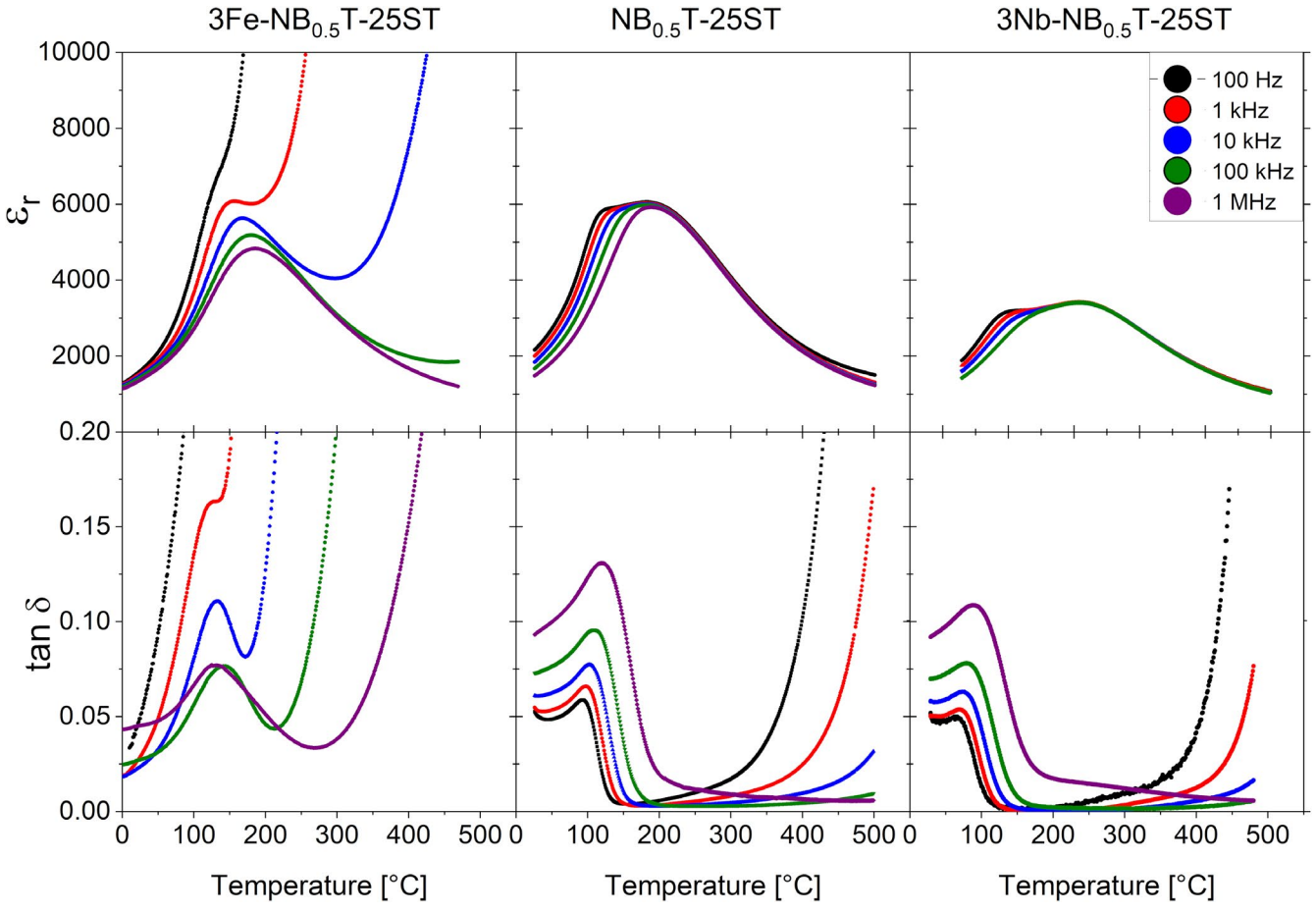

FIGURE 7 Room temperature permittivity of NBT-ST based ceramics

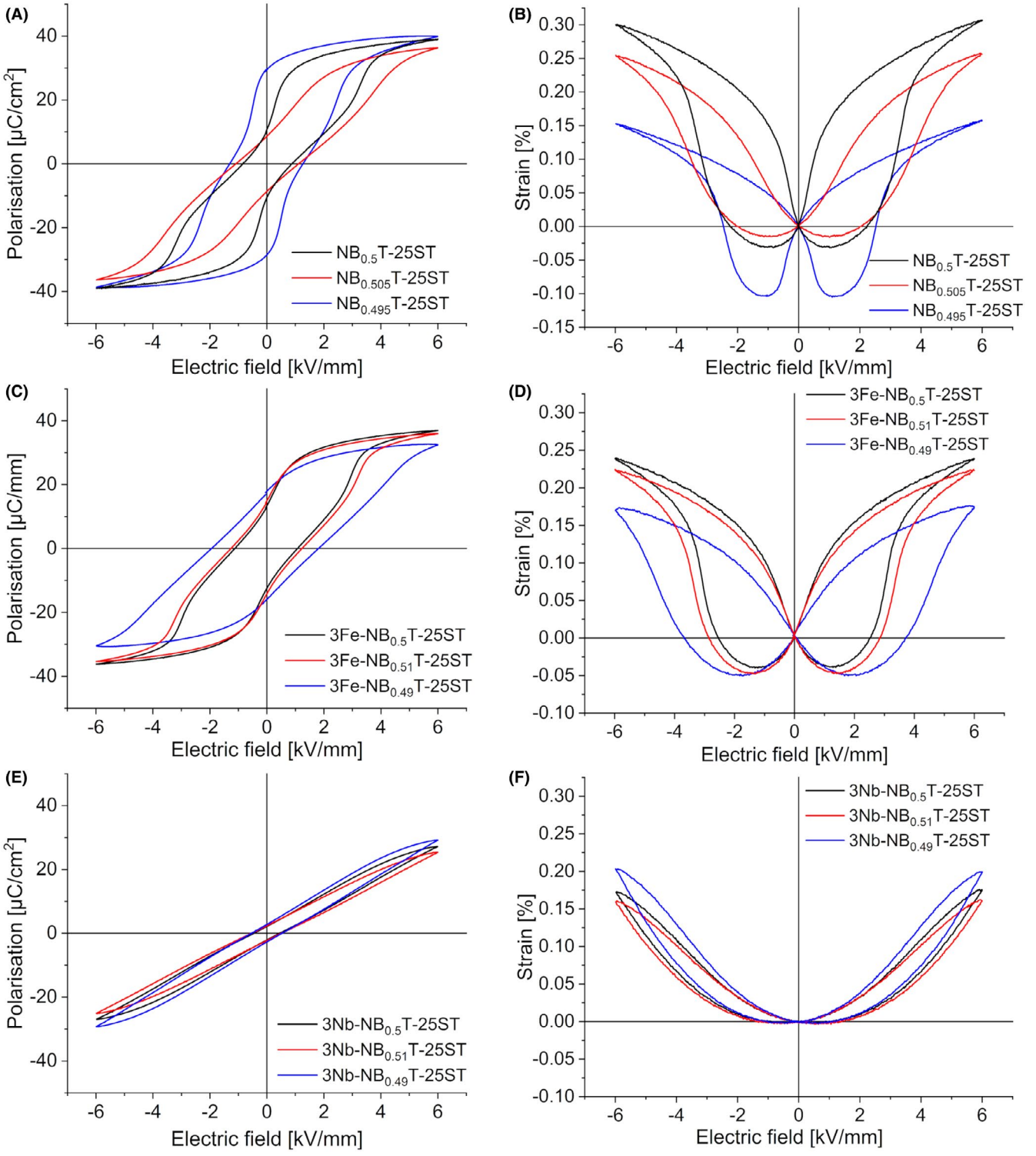

FIGURE 8 Polarization and strain loops for NBT-ST ceramics. (A) PE-loops and (B) field-dependent strain of NBT-ST with stoichiometry variations. (C) PE-loops and (D) field-dependent strain of Fe-doped NBT-ST. (E) PE-loops and (F) field-dependent strain of Nb-doped NBT-ST

from the NBT-ST. Furthermore, also, the Fe-doped samples (apart from the $NB_{0{\cdot}495}$T-25ST) show quite high strain values but with higher negative strain components. This is interesting because the 3Fe-NBT-25ST samples are all chemically homogeneous compared to NBT-25ST. This leads to two further possible conclusions. The presence of a core-shell structure may correlate with the modification of electrical properties but is not necessarily the cause of it. Additionally, the doping content influences the properties more than just changing the oxygen vacancy concentration. The last aspect can also be further

proven by evaluating the plots from the donor-doped samples. The Nb-doped materials are all rather highly polar dielectrics (Figure 8E). Neither a high remanent strain nor a pinching in the PE-plots can be observed. They furthermore hardly differ from each other. The same counts for the strain in Figure 8F. Only a parabolic dependency on the electric field can be determined, hinting toward electrostriction rather than ferroelectric strain. It could recently be shown that Nb-containing solid solutions disturb the polar structure of NBT materials.[15,44,45,46] This makes the ceramics interesting for high-temperature capacitors because the permittivity becomes constant over a wide temperature range. For obtaining anti-ferroelectric-like properties, it becomes evident that the control of the Bi-stoichiometry is still the most important parameter. Thus, a Bi-rich solid solution should be the starting point for further chemical modification of electric properties. This will also help to further elucidate the origin of the material's behavior.

4 | CONCLUSION

The formation of core-shell structures in NBT-ST is highly dependent on the oxygen vacancy concentration. This can be rationalized by a chemical diffusion couple of strontium and oxygen. Because the NBT is formed first during calcination, the chemical diffusion allows for the strontium's homogenization in the ceramic material. In the case of a low concentration of oxygen vacancies, a heterogeneous microstructure develops in the form of a core-shell structure with an NBT-rich core. The slow oxygen transport dominates the chemical diffusion in this case. The highest concentration of cores was thus reached for 3% Nb-donor doped samples. There is a drastic change in electric and ferroelectric properties depending on the existence of a core-shell structure in pure but Bi-non-stoichiometric material. This was initially seen as proof for a core-shell structure, being the cause of high strain and pinched PE-loops with low remanent polarization. However, chemically homogeneous Fe-acceptor doped samples show pinching of PE-loops and reasonably high strain as well. Therefore, the formation of a core-shell structure could be correlated with but is not necessarily the source of the observed behavior. There rather seems to be a high impact of the doping material itself on the electrical properties apart from changing the oxygen vacancy concentration. Nevertheless, the oxygen vacancy concentration remains the key to control the chemical homogeneity and will allow for finding the origin of the variation in electric properties of NBT-ST-based materials.

ACKNOWLEDGMENTS

Sebastian Steiner and Till Frömling gratefully acknowledge financial support by the Deutsche Forschungsgemeinschaft (DFG; Grant No. FR 3718/1-1). Oded Sobol and Wolfgang Unger would also like to thank the Deutsche Forschungsgemeinschaft (DFG) for funding (Grant No. UN 80/14-1).

ORCID

Till Frömling https://orcid.org/0000-0002-8827-1926

REFERENCES

1. Acosta M, Schmitt LA, Molina-Luna L, Scherrer MC, Brilz M, Webber KG, et al. Core–shell lead-free piezoelectric ceramics: current status and advanced characterization of the $Bi_{1/2}Na_{1/2}TiO_3$–$SrTiO_3$ system. J Am Ceram Soc. 2015;98(11):3405–22.
2. Koruza J, Rojas V, Molina-Luna L, Kunz U, Duerrschnabel M, Kleebe H-J, et al. Formation of the core–shell microstructure in lead-free $Bi_{1/2}Na_{1/2}TiO_3$-$SrTiO_3$ piezoceramics and its influence on the electromechanical properties. J Eur Ceram Soc. 2016;36(4):1009–16.
3. Acosta M, Schmitt LA, Cazorla C, Studer A, Zintler A, Glaum J, et al. Piezoelectricity and rotostriction through polar and non-polar coupled instabilities in bismuth-based piezoceramics. Sci Rep. 2016;6:28742.
4. Liu N, Acosta M, Wang S, Xu B-X, Stark RW, Dietz C. Revealing the core-shell interactions of a giant strain relaxor ferroelectric $0.75Bi_{1/2}Na_{1/2}TiO_3$-$0.25SrTiO_3$. Sci Rep. 2016;6:36910.
5. Thong H-C, Zhao C, Zhu Z-X, Chen X, Li J-F, Wang K. The impact of chemical heterogeneity in lead-free (K, Na)NbO_3 piezoelectric perovskite: ferroelectric phase coexistence. Acta Mater. 2019;166:551–9.
6. Zhou M, Lu X, Yang D, He J, Huang F, Mei F, et al. Induced core-shell structure and the electric properties of $(K_{0.48}Na_{0.52})_{0.95}Li_{0.05}Nb_{0.95}Sb_{0.05}O_3$ ceramics. Physical Chemistry Chemical Physics. 2017;19(3):1868–74.
7. Frömling T, Steiner S, Ayrikyan A, Bremecker D, Dürrschnabel M, Molina-Luna L, et al. Designing properties of $(Na_{1/2}Bi_x)TiO_3$-based materials through A-site non-stoichiometry. J Mater Chem C. 2018;6(4):738–44.
8. Molina-Luna L, Wang S, Pivak Y, Zintler A, Pérez-Garza HH, Spruit RG, et al. Enabling nanoscale flexoelectricity at extreme temperature by tuning cation diffusion. Nat Commun. 2018;9(1):4445.
9. Hiruma Y, Imai Y, Watanabe Y, Nagata H, Takenaka T. Large electrostrain near the phase transition temperature of $(Bi_{0.5}Na_{0.5})TiO_3$–$SrTiO_3$ ferroelectric ceramics. Appl Phys Lett. 2008;92(26):262904.
10. Wang F, Xu M, Tang Y, Wang T, Shi W, Leung CM. Large strain response in the ternary $Bi_{0.5}Na_{0.5}TiO_3$–$BaTiO_3$–$SrTiO_3$ solid solutions. J Am Ceram Soc. 2012;95(6):1955–9.
11. Maqbool A, Hussain A, Ur Rahman J, Kwon Song T, Kim W-J, Lee J, et al. Enhanced electric field-induced strain and ferroelectric behavior of $(Bi_{0.5}Na_{0.5})TiO_3$–$BaTiO_3$–$SrZrO_3$ lead-free ceramics. Ceram Int, 2014, 40(8, Part A), 11905-14.
12. Tong X-Y, Li H-L, Zhou J-J, Liu H, Fang J-Z. Giant electrostrain under low driving field in $Bi_{1/2}Na_{1/2}TiO_3$-$SrTiO_3$ ceramics for actuator applications. Ceram Int. 2016;42(14):16153–9.
13. Acosta M, Jo W, Roedel J. Temperature- and frequency-dependent properties of the $0.75Bi_{1/2}Na_{1/2}TiO_3$-$0.25SrTiO_3$ lead-free incipient piezoceramic. J Am Ceram Soc. 2014;97(6):1937–43.
14. Li J, Li F, Xu Z, Zhang S. Multilayer lead-free ceramic capacitors with ultrahigh energy density and efficiency. Adv Mater. 2018;30(32):1802155.

15. Tong X-Y, Song M-W, Zhou J-J, Wang K, Guan C-L, Liu H, et al. Enhanced energy storage properties in Nb-modified $Bi_{0.5}Na_{0.5}TiO_3$–$SrTiO_3$ lead-free electroceramics. J Mater Sci: Mater Electron, 2019.
16. Park S-E, Hong KS. Variations of structure and dielectric properties on substituting A-site cations for Sr^{2+} in $(Na_{1/2}Bi_{1/2})TiO_3$. J Mater Res. 1997;12(8):2152–7.
17. Gomah-Pettry JR, Marchet P, Salak A, Ferreira VM, Mercurio JP. Electrical properties of $Na_{0.5}Bi_{0.5}TiO_3$ – $SrTiO_3$ Ceramics. Integrated Ferroelectrics. 2004;61(1):159–62.
18. Gomah-Pettry JR, Salak AN, Marchet P, Ferreira VM, Mercurio JP. Ferroelectric relaxor behaviour of $Na_{0.5}Bi_{0.5}TiO_3$–$SrTiO_3$ ceramics. Physica Status Solidi (b). 2004;241(8):1949–56.
19. Gomah-Pettry J-R, Said S, Marchet P, Mercurio J-P. Sodium-bismuth titanate based lead-free ferroelectric materials. J Eur Ceram Soc. 2004;24(6):1165–9.
20. Rout D, Moon K-S, Kang S-JL, Kim IW. Dielectric and Raman scattering studies of phase transitions in the $(100–x)Na_{0.5}Bi_{0.5}TiO_3$–$xSrTiO_3$ system. J Appl Phys. 2010;108(8):084102.
21. Wang K, Hussain A, Jo W, Rödel J. Temperature-dependent properties of $(Bi_{1/2}Na_{1/2})TiO_3$–$(Bi_{1/2}K_{1/2})TiO_3$–$SrTiO_3$ lead-free piezoceramics. J Am Ceram Soc. 2012;95(7):2241–7.
22. Parija B, Rout SK, Cavalcante LS, Simões AZ, Panigrahi S, Longo E, et al. Structure, microstructure and dielectric properties of $100–x(Bi_{0.5}Na_{0.5})TiO_3–x[SrTiO_3]$ composites ceramics. Appl Phys A. 2012;109(3):715–23.
23. Wang F, Leung CM, Tang Y, Wang T, Shi W. Composition induced structure evolution and large strain response in ternary $Bi_{0.5}Na_{0.5}TiO_3$-$Bi_{0.5}K_{0.5}TiO_3$-$SrTiO_3$ solid solution. J Appl Phys. 2013;114(16):164105.
24. Zhao XL, Yang WZ, Liu XQ, Chen XM. Dielectric and ferroelectric characteristics of $[(Bi_{0.5}Na_{0.5})0.94Ba_{0.06}]1–xSr_xTiO_3$ ceramics. J Mater Sci: Mater Electron. 2014;25(3):1517–26.
25. Tian C, Wang F, Ye X, Xie Y, Wang T, Tang Y, et al. Bipolar fatigue-resistant behavior in ternary $Bi_{0.5}Na_{0.5}TiO_3$–$BaTiO_3$–$SrTiO_3$ solid solutions. Scripta Mater. 2014;83:25–8.
26. Li H-L, Liu Q, Zhou J-J, Wang K, Li J-F, Liu H, et al. Grain size dependent electrostrain in $Bi_{1/2}Na_{1/2}TiO_3$-$SrTiO_3$ incipient piezoceramics. J Eur Ceram Soc. 2016;36(11):2849–53.
27. Kim S, Choi H, Han S, Park JS, Lee MH, Song TK, et al. A correlation between piezoelectric response and crystallographic structural parameter observed in lead-free $(1–x)(Bi_{0.5}Na_{0.5})TiO_3$–$xSrTiO_3$ piezoelectrics. J Eur Ceram Soc. 2017;37(4):1379–86.
28. Lee J-K, Hong KS, Kim CK, Park S-E. Phase transitions and dielectric properties in A-site ion substituted $(Na_{1/2}Bi_{1/2})TiO_3$ ceramics (A = Pb and Sr). J Appl Phys. 2002;91(7):4538–42.
29. Mgbemere HE, Fernandes RP, Schneider GA. Structure and electrical properties of $0.85(Bi_{0.5}Na_{0.5})TiO_3$–$0.12BaTiO_3$–$0.03SrTiO_3$ ferroelectric ceramics. J Eur Ceram Soc. 2013;33(15–16):3015–22.
30. Li M, Pietrowski MJ, De Souza RA, Zhang H, Reaney IM, Cook SN, et al. A family of oxide ion conductors based on the ferroelectric perovskite $Na_{0.5}Bi_{0.5}TiO_3$. Nat Mater. 2014;13(1):31–5.
31. Li M, Zhang H, Cook SN, Li L, Kilner JA, Reaney IM, et al. Dramatic influence of A-site nonstoichiometry on the electrical conductivity and conduction mechanisms in the perovskite oxide $Na_{0.5}Bi_{0.5}TiO_3$. Chem Mater. 2015;27(2):629–34.
32. Yang F, Zhang H, Li L, Reaney IM, Sinclair DC. High ionic conductivity with low degradation in A-site strontium-doped non-stoichiometric sodium bismuth titanate perovskite. Chem Mater. 2016;28(15):5269–73.
33. Koch L, Steiner S, Meyer K-C, Seo I-T, Albe K, Fromling T. Ionic conductivity of acceptor doped sodium bismuth titanate: influence of dopants, phase transitions and defect associates. J Mater Chem C. 2017;5(35):8958–65.
34. Steiner S, Seo I-T, Ren P, Li M, Keeble DJ, Frömling T. The effect of Fe-acceptor doping on the electrical properties of $Na_{1/2}Bi_{1/2}TiO_3$ and $0.94(Na_{1/2}Bi_{1/2})TiO_3$-0.06 $BaTiO_3$. J Am Ceram Soc. 2019;102(9):5295–304.
35. Groszewicz PB, Koch L, Steiner S, Ayrikyan A, Webber KG, Frömling T, et al. The fate of aluminium in (Na, Bi)TiO_3-based ionic conductors. J Mater Chem A. 2020;8(35):18188–97.
36. Ren P, Gehringer M, Huang B, Hoang A-P, Steiner S, Klein A, et al. High field electroformation of sodium bismuth titanate and its solid solutions with barium titanate. J Mater Chem C, 2021.
37. Holzlechner G, Kubicek M, Hutter H, Fleig J. A novel ToF-SIMS operation mode for improved accuracy and lateral resolution of oxygen isotope measurements on oxides. J Anal At Spectrom. 2013;28(7):1080–9.
38. Krauss W, Schütz D, Mautner FA, Feteira A, Reichmann K. Piezoelectric properties and phase transition temperatures of the solid solution of $(1–x)(Bi_{0.5}Na_{0.5})TiO_{3–x}SrTiO_3$. J Eur Ceram Soc. 2010;30(8):1827–32.
39. Sayyed S, Acharya SA, Kautkar P, Sathe V. Structural and dielectric anomalies near the MPB region of $Na_{0.5}Bi_{0.5}TiO_3$–$SrTiO_3$ solid solution. RSC Advances. 2015;5(63):50644–54.
40. Cao WP, Li WL, Dai XF, Zhang TD, Sheng J, Hou YF, et al. Large electrocaloric response and high energy-storage properties over a broad temperature range in lead-free NBT-ST ceramics. J Eur Ceram Soc. 2016;36(3):593–600.
41. Irvine JTS, Sinclair DC, West AR. Electroceramics: characterization by impedance spectroscopy. Adv Mater. 1990;2(3):132–8.
42. Sinclair DC, West AR. Electrical properties of a $LiTaO_3$ single crystal. Physical Review B. 1989;39(18):13486–92.
43. East J, Sinclair DC. Characterization of $(Bi_{1/2}Na_{1/2})TiO_3$ using electric modulus spectroscopy. J Mater Sci Lett. 1997;16(6):422–5.
44. Shen ZB, Wang XH, Song DS, Li LT. Nb-doped $BaTiO_3$-$(Bi_{0.5}Na_{0.5})TiO_3$ ceramics with core-shell structure for high-temperature dielectric applications. Adv Appl Ceram. 2016;115(7):435–42.
45. Xu Q, Song Z, Tang W, Hao H, Zhang L, Appiah M, et al. Ultra-wide temperature stable dielectrics based on $Bi_{0.5}Na_{0.5}TiO_3$–$NaNbO_3$ system. J Am Ceram Soc. 2015;98(10):3119–26.
46. Yao G, Wang X, Wu Y, Li L. Nb-doped $0.9BaTiO_3$–$0.1(Bi_{0.5}Na_{0.5})TiO_3$ ceramics with stable dielectric properties at high temperature. J Am Ceram Soc. 2012;95(2):614–8.

SUPPORTING INFORMATION

Additional supporting information may be found online in the Supporting Information section.

How to cite this article: Steiner S, Heldt J, Sobol O, Unger W, Frömling T. Influence of oxygen vacancies on core-shell formation in solid solutions of (Na,Bi)TiO_3 and $SrTiO_3$. *J Am Ceram Soc*. 2021;00:1–10. https://doi.org/10.1111/jace.17845